Chemical Engineering Science 123 (2015) 92–98

Contents lists available at ScienceDirect

Chemical Engineering Science

journal homepage: www.elsevier.com/locate/ces

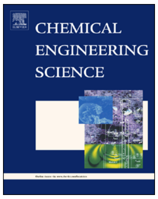

Numerical analysis of strain rate sensitivity in ball indentation on cohesive powder Beds

M. Pasha, C. Hare, A. Hassanpour, M. Ghadiri*

Institute of Particle Science and Engineering, University of Leeds, Leeds, LS2 9JT, UK

HIGHLIGHTS

- Flowability of cohesive powders in the intermediate range of strain rates has been investigated.
- Effects of strain rate on bed hardness is analysed using DEM.
- Stresses are almost constant up to a dimensionless strain rate of 1.
- For dimensionless strain rates greater than 1, the stresses become rate dependent.
- Fluctuations in the stresses are negligible in the quasi-static regime, but not beyond.

GRAPHICAL ABSTRACT

Stresses become strain rate dependent for dimensionless strain rates greater than unity. Below this limit the quasi-static regime is observed. There are notable fluctuations beyond the quasi-static regime, and the data presented here are averaged.

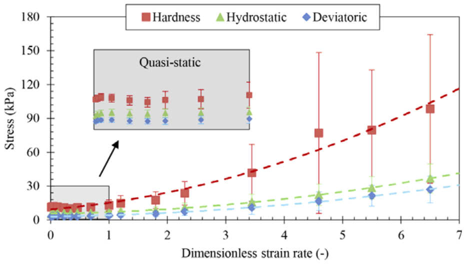

ARTICLE INFO

Article history:
Received 10 January 2014
Received in revised form
13 October 2014
Accepted 14 October 2014
Available online 27 October 2014

Keywords:
Flowability
DEM
Indentation on powder bed
Strain rate
Cohesive powder

ABSTRACT

In the shear deformation of powder beds beyond the quasi-static regime the shear stress is dependent on the strain rate. Extensive work has been reported on the rapid chute flow of large granules but the intermediate regime has not been widely addressed particularly in the case of cohesive powders. However in industrial powder processes the powder flow is often in the intermediate regime. In the present work an attempt is made to investigate the sensitivity of the stresses in an assembly of cohesive spherical particles to the strain rate in ball indentation using the Distinct Element Method. This technique has recently been proposed as a quick and easy way to assess the flowability of cohesive powders. It is shown that the hardness, deviatoric and hydrostatic stresses within a bed, subjected to ball indentation on its free surface, are dependent on the indentation strain rate. These stresses are almost constant up to a dimensionless strain rate of unity, consistent with trends from traditional methods of shear cell testing, though fluctuations begin to increase from a dimensionless strain rate of 0.5. For dimensionless strain rates greater than unity, these stresses increase, with the increase in hardness being the most substantial. These trends correlate well with those established in the literature for the Couette device. However the quantitative value of the strain rate boundary of the regimes differs, due to differences in the geometry of shear deformation bands. Nevertheless, this shows the capability of the indentation technique in capturing the dynamics of cohesive powder flow.

1. Introduction

In industrial processes such as mixing, blending, handling and storage reliable powder flow is important for product quality and a consistent production rate. Understanding the flow characteristics of the powder can avoid wastage, machinery maintenance problems

---

* Corresponding author. Tel.: +44 113 343 2406; fax: +44 113 343 2405.
E-mail address: M.Ghadiri@leeds.ac.uk (M. Ghadiri).

http://dx.doi.org/10.1016/j.ces.2014.10.026

and downtime in such processes. Strain rate is particularly of great importance since in the shear deformation of powder beds beyond the quasi-static regime the shear stress is dependent on the strain rate (Tardos et al., 2003). Extensive work has been reported on the rapid chute flow of large granules (Savage, 1979) but the intermediate regime has not been widely addressed, particularly for cohesive powders. However in industrial powder processes the powder flow is often in the intermediate regime, for which the specification of an operational window in terms of strain rate for reliability and control is highly desirable. Tardos et al. (2003) classified powder flow into three regimes based on the shear strain rate of the process. At very low strain rates, the frictional forces between particles are predominant and the shear stress is independent of the strain rate, hence this is termed the quasi-static regime. In the other extreme at very high strain rates, that is, the dynamic regime, the flow is characterised by rapid and short duration collisions between particles rather than the friction between them and hence the particle inertia is influential. There has been extensive work for this regime, in which it has been shown that the shear stress varies with the square of strain rate (Savage and Sayed, 1984; Bagnold, 1954; Campbell and Brennen, 1985). Between the quasi-static and dynamic, inertial regimes lies the intermediate regime, where both collisional and frictional interactions between the particles influence the flow characteristics (Tardos et al., 2003). There exist a number of test methods for evaluation of flow behaviour of powders, such as the unconfined compression test (Parrella et al., 2008), shear test (Schulze, 1994) and a few recently developed techniques, such as the Sevilla powder tester (Castellanos et al., 2004) the raining bed technique (Formisani et al., 2002) and the ball indentation method (Hassanpour and Ghadiri, 2007). All of these methods evaluate the incipient flow at very low strain rates (i.e. the quasi-static regime), and hence cannot depict the strain rate sensitivity of powder flow. The only method by which the intermediate regime has been analysed is the Couette device of Tardos et al. (2003), where the powder is sheared between two concentric cylinders (with the axis being vertical). The inner cylinder is rotated at different rotational velocities whilst the outer cylinder is stationary, forming a shear band in the gap. It was confirmed that during the quasi-static regime the stresses were independent of the strain rate. For the intermediate regime the dependency of the shear stress on the dimensionless strain rate γ^* (as given by Eq. (1)) is with a power index less than 2.

$$\gamma^* = \gamma \left(\frac{d_p}{g}\right)^{1/2} \tag{1}$$

where γ is the strain rate, d_p is the mean particle diameter and g is the gravitational acceleration. For the dynamic regime, this dependency is to the power 2 (Savage and McKeown, 1983). Tardos et al. (2003) observed that the fluctuations of the stresses increased with the strain rate and that the width of the intermediate regime in terms of dimensionless strain rate was a function of the assembly concentration (Tardos et al., 2003). At low particle concentrations (high bed porosity), the width was relatively narrow, between dimensionless rates of 0.5 to 2 (Tardos et al., 2003).

In two commercial instruments the powder is also subjected to shear strains in the intermediate regime by a paddle penetrating whilst rotating in a powder bed (Freeman Powder Tester FT4 (Freeman, 2007; Bharadwaj et al., 2010) and PowderFlow Analyser by StableMicro Systems, Surrey, UK). However the complex paddle geometry provides a highly non-uniform strain field, where the powder strain and strain rate increase from the centre to the cylindrical wall. Recently Hare et al. (2011) have analysed the shear stress and strain fields around a rotating impeller and have quantified their radial and axial variations. Their work shows that the shear stresses are greatest in the vicinity of the front of the blades; the stresses reduce above the impeller and away from the impeller in the angular direction, providing a highly non-uniform strain field. Based on their work, the interpretation of paddle torque to elucidate the strain rate dependency of shear stresses using these commercial devices is difficult until systematic work on model materials with 'tuneable' and controlled bulk cohesion has been fully analysed.

Moreno-Atanasio et al. (2005) simulated uniaxial unconfined compression of cohesive beds using the Distinct Element Method (DEM) for a range of strain rates. They also found that the unconfined yield stress (UYS) did not depend on strain rate for small values of strain rate (less than 2 s^{-1}), and only exhibited dependency for larger values, where a linear relationship between UYS and strain rate was reported. A power law fit with a power index of 1.2 showed the best fit for the simulations data. The threshold strain rate which defined the limiting quasi-static rate was found to be slightly dependent on the inter-particle cohesion, where by increasing the cohesion the threshold was increased slightly. It was also shown that by increasing the pre-consolidation stress, the sensitivity of UYS to the strain rate decreased in the intermediate and inertial regimes, which is in-line with Tardos et al. (2003) findings on assembly concentration. It should be noted that possible effects of aeration were not considered in the above analysis.

In the present work an attempt is made to investigate the sensitivity of the stresses in an assembly of cohesive spherical particles in the ball indentation process (Pasha et al., 2013) using DEM. Again, the effect of air drag in this analysis is ignored.

1.1. Ball indentation technique

Hassanpour and Ghadiri (2007) proposed a test method for assessing the flowability of cohesive powders based on ball indentation on a powder bed. The method has a unique advantage as it can be performed on small amounts of loosely compacted powders. For the experimental indentation process, a powder sample is lightly consolidated into a cylindrical die which is made of low friction materials in order to reduce the effects of wall friction. The surface of the consolidated bed is then indented using a spherical indenter and the depth/load cycle is recorded from which the 'hardness' of the powder surface is inferred. For continuum solids, hardness represents the flow stress following a certain extent of strain (Tabor, 2000). The same approach has been explored for particulate solids by Wang et al. (2008), where it has been shown that the flow stress obtained by this method correlates well with the unconfined yield stress measurements obtained from shear cell and unconfined uniaxial compression test methods. Here we use the terms hardness and flow stress interchangeably. Hardness, H, is given by the ratio of the maximum indentation load, F, to the projected area of the impression,

$$H = \frac{F}{A} \tag{2}$$

where A is the area of the base of the spherical cap that is formed by the impression. The projected area can be expressed in terms of the size of the indenter and depth of impression:

$$A = \pi(dh - h^2) \tag{3}$$

where d is the indenter diameter and h is the depth of impression.

2. DEM simulation of ball indentation process

For the analysis of contact force distribution and the resulting stresses in an assembly of particulate solids, the most appropriate approach is the use of computer simulations by DEM. Details on the methodology and its applications are presented elsewhere (Cundall and Strack, 1979; Zhu et al., 2008). Pasha et al. (2013) investigated the criteria which defined the minimum required sample quantity and the suitable indenter size range for the ball indentation method using DEM simulations. It was found that a minimum dimensionless penetration (ratio of penetration depth to indenter radius) of 0.1 was required in order to initiate a plastic flow in the assembly. It was shown that a minimum bed height and a minimum bed diameter of 20 and 45 particle diameter ratios, respectively, were required in order to achieve reliable measurements of hardness. A sensitivity analysis of indenter size revealed that indenter to particle diameter ratios smaller than 16 exhibited fluctuations in powder flow stress measurements, which did not represent shear deformation. Larger indenters provided stable values for flow stress, subject to the minimum sample criteria being met (Pasha et al., 2013). In the present work, the simulations are based on meeting the criteria defined by Pasha et al. (2013). The ratios of sample height and sample diameter to particle diameter are 20 and 45, respectively. The dynamic indentation process was simulated using a 16 mm diameter indenter.

The simulations are conducted using EDEM® software provided by DEM Solutions, Edinburgh, UK. The normal and tangential contact forces are evaluated based on the special case of the linear elasto-plastic and adhesive model of Pasha et al. (2014), as shown in Fig. 1. In this model, when two adhesive spheres come into contact, the normal force drops to a certain negative value, $8f_{ce}/9$, where f_{ce} is the JKR (Johnson et al., 1971) pull-off force given by Eq. (4),

$$f_{ce} = \frac{3}{2}\pi R^* \Gamma \tag{4}$$

where R^* is the reduced radius given by Eq. (5) and Γ is the interface energy.

$$R^* = \left(\frac{1}{R_1} + \frac{1}{R_2}\right)^{-1} \tag{5}$$

where R_1 and R_2 are the radii of the spheres in contact. On initial compressive loading, the contact is considered to be plastically deforming with a stiffness (slope) k_p (see Fig. 1) to a maximum overlap of α_{max}. The unloading is fully elastic, during which the force drops on a line with slope k_e. Unloading below α_p (overlap at which the contact force becomes zero) produces an adhesive force until the pull-off force (i.e. maximum tensile force), f_{cp}, is reached at the overlap α_{cp}. Further unloading leads to a reduction in the attractive force, with a slope -k_e until detachment occurs at overlap α_{fp}, where the contact force is $5f_{cp}/9$. The increase in the pull-off force due to increased plastic deformation in this model is governed by the plastic-adhesive stiffness, k_{cp}. Reloading at any instant leads to an increase of the force along the same line, that is, the line with slope -k_e and k_e for overlaps smaller than α_{cp} and α_{max}, respectively, until the previous maximum force is reached; if α increases further beyond α_{max}, the force again follows the line with slope k_p and α_{max} is adjusted accordingly (Pasha et al., 2014).

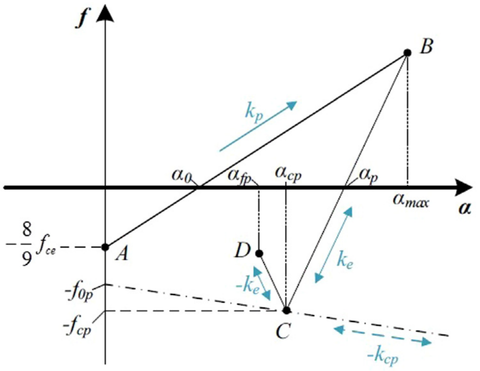

Fig. 1. Special case of the linear elasto-plastic and adhesive contact model of Pasha et al. (2014).

The tangential force calculation of this model is based on a linear tangential stiffness, k_t,

$$f_t = k_t \alpha_t \tag{6}$$

where α_t is the tangential displacement. The sliding criteria considers a contribution from the adhesive force based on the work of Savkoor and Briggs, (1977), and Thornton and Yin, (1991), as given by,

$$f_t \le \mu\left(|f_n| + 2|f_{cp}|\right) \tag{7}$$

where μ is the coefficient of sliding friction, f_n is the normal contact force and f_{cp} is the pull-off force.

Particles with a normal size distribution (d_{min}=0.896 mm and d_{max}=1.410 mm) and a mean diameter of 1 mm (as shown in Table 1) are generated inside a cylindrical die with a diameter of 45 mm. The use of a poly disperse particle population rather than a perfectly mono disperse population would avoid the formation of ordered packing. In order to provide a bed height of approximately 20 mm, 29000 particles are generated.

The tangential stiffness, k_t, was equated to the elastic stiffness, k_e, throughout the simulations, following Cundall and Strack, (1979), who showed that for elastic bodies in contact with elliptical contact areas, the ratio of tangential to normal stiffness is in a range from 2/3 to 1. The material and interactional properties of the particles and geometries are summarised in Tables 2 and 3.

Table 1
Size distribution of the generated particles.

Particle Diameter (mm)	Number Frequency (%)
0.724	3.87
0.814	11.31
0.896	21.14
1.000	27.92
1.104	20.99
1.188	11.02
1.278	3.76

Table 2
Material properties used in the simulations.

Material Property	Particles	Geometries
Envelope density (kg/m^3)	2500	7800
Poisson's ratio (dimensionless)	0.25	0.3
Elastic stiffness, k_e (MN/m)	1	8
Plastic stiffness, k_p (MN/m)	0.1	–
Plastic-adhesive stiffness, k_{cp} (MN/m)	0.01	–

Table 3
Interaction properties used in the simulations.

Interactional Property	Particle-Particle	Particle-Wall
Coefficient of restitution	0.5	0.3
Coefficient of sliding friction	0.15	0
Coefficient of rolling friction	0.01	0
Interface energy (J m^{-2})	2.0	0

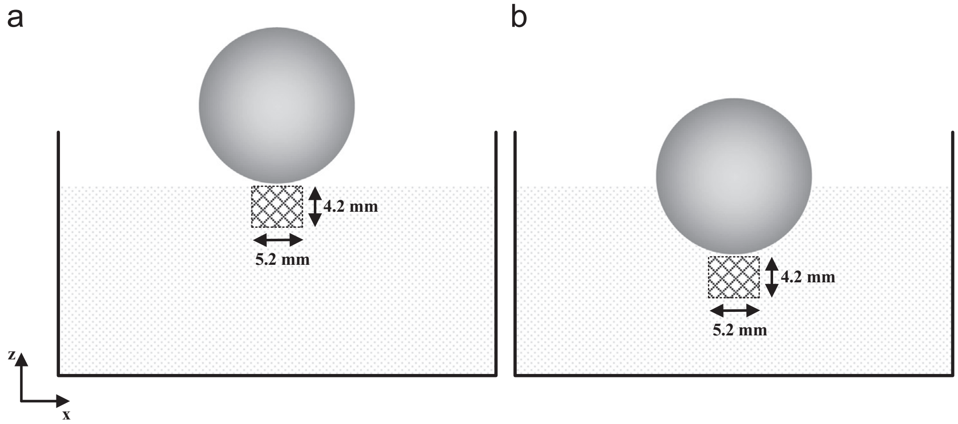

Fig. 2. Schematic diagram of the dynamic bin underneath the indenter at two different penetration depths.

The particles are assumed to be elasto-plastic and adhesive spheres whereas the die walls and the indenter are assumed to be perfectly elastic. The particles are generated within the die, ascribed the properties as given in Tables 1–3 and allowed to settle under gravity. The assembly is then consolidated with a piston at a constant strain rate of 1 s^{-1} to 10 kPa. Once the desired stress is achieved, the piston is unloaded at the same speed (0.0192 m/s) as that of the loading, but with opposite direction. The reason for 10 kPa pre-consolidation load being applied is that it is within the realistic range of experimental work, where results of other flowability techniques, e.g. uniaxial unconfined compression, have been reported. The indentation process on the pre-consolidated assembly is simulated for a range of strain rates. The indentation strain rate, γ, is considered to be the rate of penetration divided by the radius of the indenter as described in Eq. (8),

$$\gamma = \frac{v_i}{r_i} \tag{8}$$

where v_i is the indenter speed and r_i is the indenter radius. The strain rate is made dimensionless using Eq. (1). The range of dimensionless strain rates analysed is from 0.0115 to 6.5 (equivalent to indenter speeds of 0.009 to 5.15 m/s). In order to analyse the internal stresses, a similar approach to the previous work of Pasha et al. (2013) is considered, where the hydrostatic and deviatoric stresses inside a dynamic cuboid bin just below the indenter (see Fig. 2) are calculated. This bin has dimensions of 5.2, 5.2 and 4.2 mm in x, y and z directions, respectively, while its position is fixed relative to the indenter, that is, it moves with the indenter (see Fig. 2).

The forces acting on each particle whose centre was inside this bin are calculated and the components of the stress tensor within the bin were evaluated using Eq. (9),

$$\sigma_{ij} = -\frac{1}{V}\sum_{N_p}\sum_{N_c}|x_i^c - x_i^p| n_i F_j \tag{9}$$

where σ_{ij} is the *ij*-component of the stress tensor, *V* is the volume of the bin, N_p is the number of particles in the bin, N_c is the number of contacts around particle *p*, and x_i^c, x_i^p and n_i are the *i*-components of contact location, particle centre and normal vector directed from a particle centroid to its contact, respectively, and F_j is the *j*-component of the contact force (Bagi, 1996). The hydrostatic, σ_{hyd}, and deviatoric, τ_D, stresses are evaluated from normal stresses using Eqs. (10) and (11), respectively (Luding, 2008),

$$\sigma_{hyd} = \frac{\sigma_1 + \sigma_2 + \sigma_3}{3} \tag{10}$$

$$\tau_D = \left(\frac{(\sigma_1 - \sigma_2)^2 + (\sigma_1 - \sigma_3)^2 + (\sigma_2 - \sigma_3)^2}{6}\right)^{1/2} \tag{11}$$

where σ_1, σ_2 and σ_3 are the principal stresses.

3. Results and Discussion

The hardness, hydrostatic and deviatoric stresses inside the dynamic bin are shown in Fig. 3(a)-(d) as functions of dimensionless penetration for dimensionless strain rates of 0.01, 0.23, 0.46 and 2.30, respectively. As it can be seen, by increasing the strain rate the fluctuations become more significant. This is in line with the findings of Tardos et al. (2003), who showed that by increasing the strain rate large fluctuations appeared and a “liquid-like” viscous character was manifested by the bulk powder. With higher strain rates, a larger average value of hardness is evaluated, although the fluctuations are influential in determining this average. These results are logically consistent as the flow stress (hardness) is larger than the other two stress types due to the ball indentation being constrained (Tabor, 2000). Also the hydrostatic stress is larger than the deviatoric stress, as the deformation is active and σ_{zz}â ª ¢σ_{xx} or σ_{yy}. Additionally, the dominance of particle inertia reduces the influence of frictional contributions and the difference between the hydrostatic and deviatoric stresses reduces.

In order to facilitate further observations, the hardness, hydrostatic and deviatoric stresses inside the dynamic bin under the indenter are shown in Fig. 4(a)-(c), respectively, as a function of dimensionless penetration for the four dimensionless strain rates. A close examination of these figures indicates a threshold strain rate above which the stresses in the system increase substantially.

In order to specify this threshold in terms of the dimensionless strain rate, a wide range of indentation speeds were simulated and analysed. The hardness, hydrostatic and deviatoric stresses inside the dynamic bin are plotted in Fig. 5 as functions of γ^* with the error bars indicating the standard deviation of the fluctuations. As it can be seen, the stresses are insensitive to strain rate variations for small indenter speeds up to a dimensionless strain rate of about unity, beyond which the stresses start increasing. The error bars also decrease in width with the lowering of the strain rate, in line with Tardos et al., (2003) work, where it was found that the dynamic and quasi-static regimes reached asymptotically to the limits of large and small fluctuations, respectively.

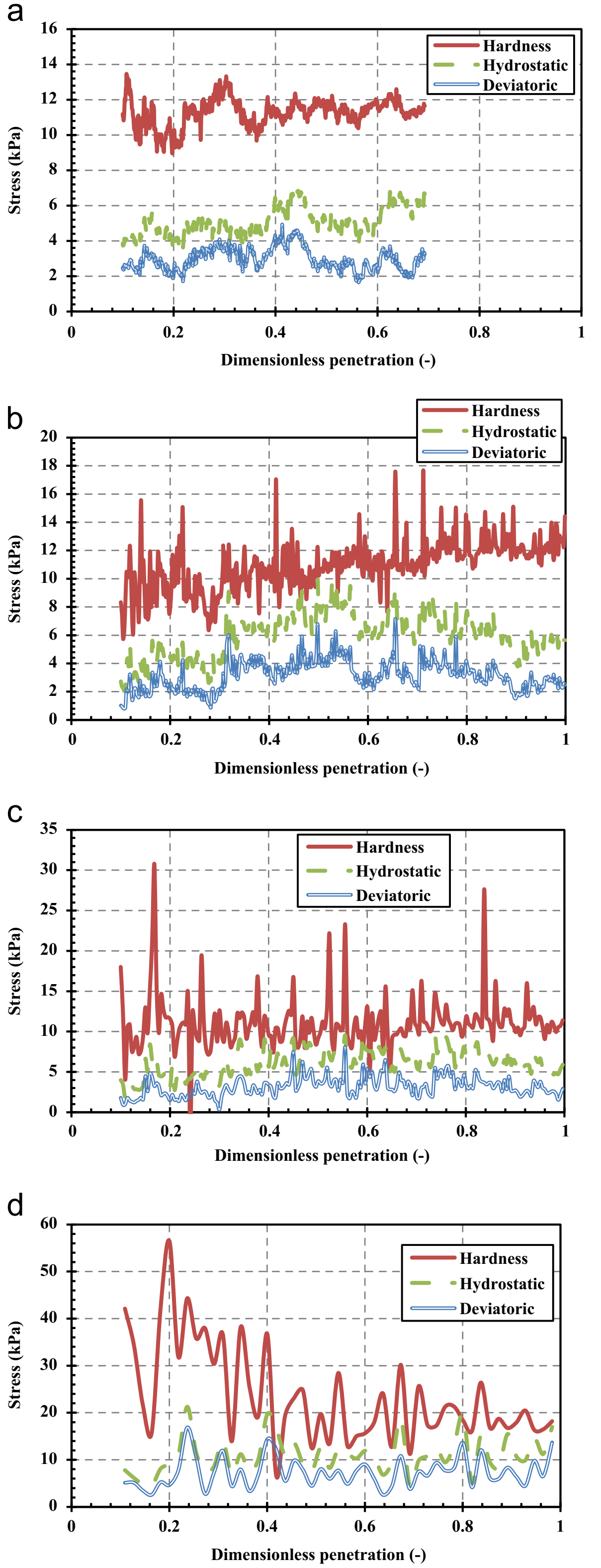

Fig. 3. Hardness, hydrostatic and deviatoric stresses inside the dynamic bin as functions of dimensionless penetration for a number of dimensionless strain rates in the range 0.01–2.30. (a) $\gamma^*=0.01$, (b) $\gamma^*=0.23$, (c) $\gamma^*=0.46$ and (d) $\gamma^*=2.30$.

Fig. 6 shows the hardness, hydrostatic and deviatoric stresses inside the dynamic bin as functions of γ^* for values $\gamma^* < 1$, with the error bars indicating the standard deviation of the fluctuations.

As it can be seen, the stresses are relatively independent of the strain rate for this range, though the fluctuations increase with γ^*.

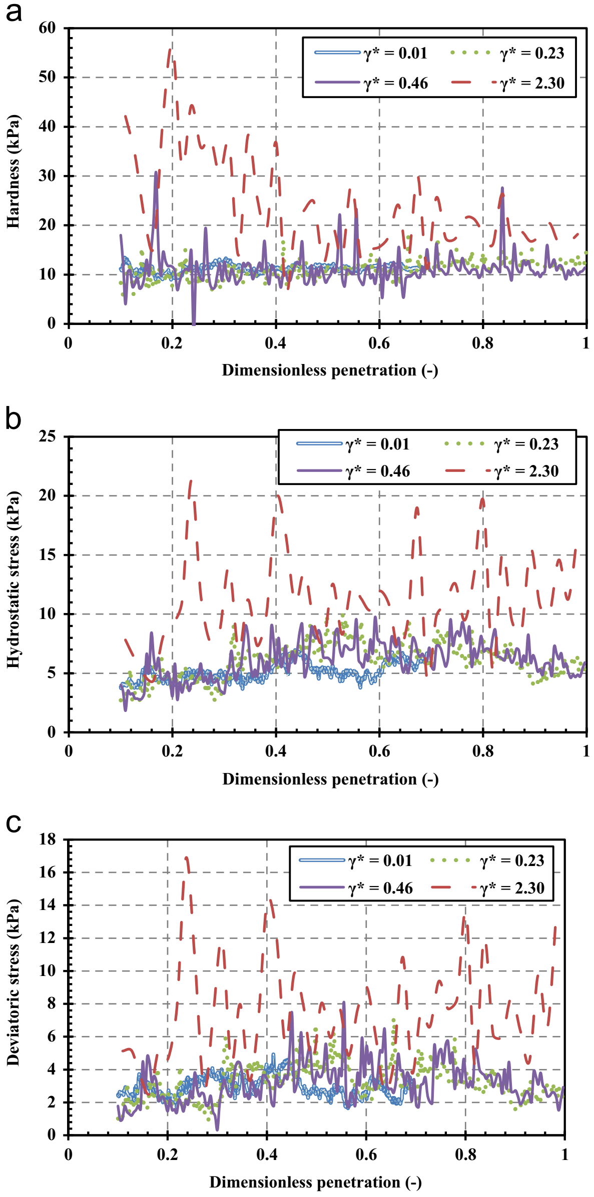

Fig. 4. (a) Hardness, (b) hydrostatic and (c) deviatoric stresses inside the dynamic bin as functions of dimensionless penetration for four of dimensionless strain rates in the range 0.01–2.30.

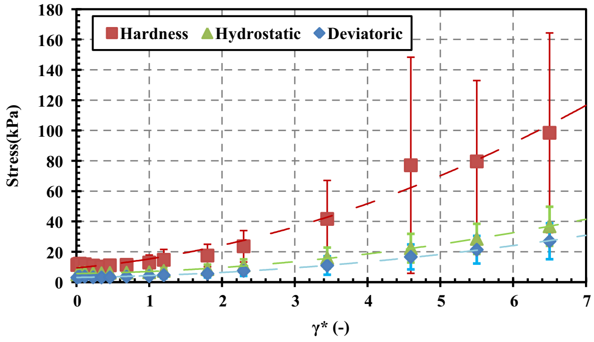

Fig. 5. Hardness, hydrostatic and deviatoric stresses inside the dynamic bin as functions of dimensionless strain rate with the error bars indicating the standard deviation of the fluctuations.

It is noteworthy that the ratio of hardness over the internal stresses is constant for $\gamma^* < 1$ (see Fig. 6), but it changes with the strain rate above this threshold (see Fig. 5), implying that the flow

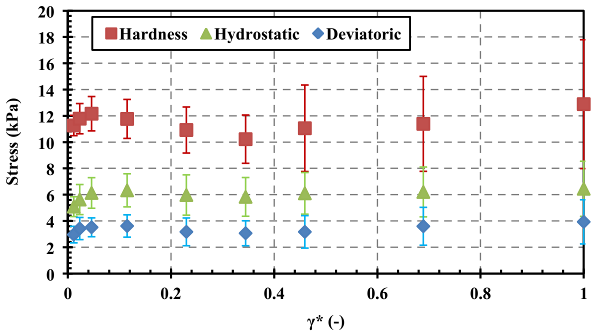

Fig. 6. Hardness, hydrostatic and deviatoric stresses inside the dynamic bin as functions of dimensionless strain rate.

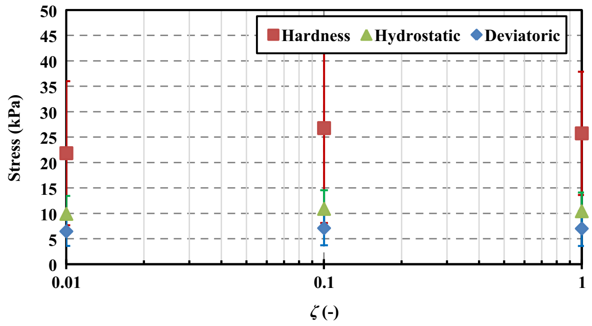

Fig. 7. Hardness, hydrostatic and deviatoric stresses inside the dynamic bin as functions of ζ.

stress, as expressed by the indentation hardness, becomes strain rate dependent at high strain rates.

The strain rate dependency is a matter of particle inertia, giving rise to different force transmission fabric, and should hence be independent of the integration time-step. In order to check this, the integration time-step was varied and the stress profile analysed. The integration time-step is calculated based on a mass-spring system which is given by Eq. (12).

$$\Delta t = \sqrt{\frac{m^*}{k^*}} \tag{12}$$

where m^* is the equivalent mass of the smallest particle given by Eq. (13), and k^* is the largest equivalent stiffness in the system given by Eq. (14).

$$m^* = \frac{m_{smallest}}{2} \tag{13}$$

where $m_{smallest}$ is the mass of the smallest particle in the system.

$$k^* = \frac{k_{\mathrm{largest}}}{2} \tag{14}$$

where $k_{largest}$ is the largest stiffness in the system. In order to investigate the dependency of the simulation results on the time-step, the simulation of the indentation process with the dimensionless strain rate of 2.30 (i.e. large strain rate) was performed using different time-steps. The time-step is calculated using Eq. (15).

$$\Delta t_d = \zeta . \Delta t \tag{15}$$

where ζ is the fraction of the critical time-step and Δt is the critical time-step evaluated based on the mass-spring theory using Eq. (12). The average values and standard deviations of hardness, deviatoric and hydrostatic stresses are plotted in Fig. 7 as a function of ζ.

The results of the hydrostatic and deviatoric stresses are insensitive to the time-step for the range investigated here. However, the average value of hardness is slightly smaller for the fraction of the time-step 0.01 as compared to 0.10 and 1.00. This difference is still negligible relative to the magnitude of the deviations in the system. It can therefore be concluded that the influence of strain rate on the stresses occurring in an assembly of cohesive spheres subjected to ball indentation, as observed here, is not an artefact of the time-step.

4. Conclusions

The hardness, deviatoric and hydrostatic stresses of a bed of cohesive spheres subjected to ball indentation have been analysed as a function of the indentation strain rate for the first time. These stresses are almost constant up to a dimensionless strain rate of 1, though fluctuations begin to increase from $\gamma^*=0.5$. However, when γ^* is greater than 1, these stresses start increasing with γ^*, with the increase in hardness being the most substantial. The information obtained here corroborates the trend already reported in the literature (Tardos et al., 2003; Savage, 1979; Savage and Sayed, 1984; Bagnold, 1954; Campbell and Brennen, 1985) and confirms that the ball indentation technique can be used to analyse powder flowability in a wide range of strain rates in a quick and easy way, with the added advantage that only a small quantity of powder is required.

Acknowledgments

The financial support of the Engineering and Physical Sciences Research Council, UK, through the Grant EP/G013047 is gratefully acknowledged.

References

Bagi, K., 1996. Stress and strain in granular assemblies. Mech. Mater. 22, 165–177.
Bagnold, R.A., 1954. Experiments on a gravity-free dispersion of large solid spheres in a newtonian fluid under shear. P. Roy. Soc. Lond. Ser. A. Mat. Phys. Sci. 225, 49–63.
Bharadwaj, R., Ketterhagen, W.R., Hancock, B.C., 2010. Discrete element simulation study of a freeman powder rheometer. Chem. Eng. Sci. 65, 5747–5756.
Campbell, C.S., Brennen, C.E., 1985. Computer simulation of granular shear flows. J. Fluid Mech. 151, 167–188.
Castellanos, A., Valverde, J.M., Quintanilla, M.A.S., 2004. The sevilla powder tester: a tool for characterizing the physical properties of fine cohesive powders at very small consolidations. Kona 22, 66–81.
Cundall, P.A., Strack, O.D.L., 1979. A discrete numerical model for granular assemblies. Geotechnique 29, 47–65.
Formisani, B., Bernado, P., Girimonte, R., Minnicelli, A. 2002, The bed support experiment in the analysis of the fluidization properties of fine solids, 4th World Congress on Particle Technology, Sydney, Australia, 21–26.
Freeman, R., 2007. Measuring the flow properties of consolidated, conditioned and aerated powders — a comparative study using a powder rheometer and a rotational shear cell. Powder Technol. 174, 25–33.
Hare, C., Ghadiri, M., Dennehy, R., 2011. Prediction of attrition in agitated particle beds. Chem. Eng. Sci. 66, 4757–4770.
Hassanpour, A., Ghadiri, M., 2007. Characterisation of flowability of loosely compacted cohesive powders by indentation. Part. Part. Syst. Char. 24, 117–123.
Johnson, K.L., Kendall, K., Roberts, A.D., 1971. Surface energy and the contact of elastic solids. P. Roy. Soc. Lond. A. Mat. Phys. Sci. 324, 301–313.
Luding, S., 2008. Constitutive relations for the shear band evolution in granular matter under large strain. Particuology 6, 501–505.
Moreno-Atanasio, R., Antony, S.J., Ghadiri, M., 2005. Analysis of flowability of cohesive powders using Distinct Element Method. Powder Technol. 158, 51–57.
Parrella, L., Barletta, D., Boerefijin, R., Poletto, M., 2008. Comparison between a uniaxial compaction tester and a shear tester for the characterisation of powder flowability. KONA Powder Part. J. 26, 178–189.
Pasha, M., Hare, C., Hassanpour, A., Ghadiri, M., 2013. Analysis of ball indentation on cohesive powder beds using distinct element modelling. Powder Technol. 233, 80–90.
Pasha, M., Dogbe, S., Hare, C., Hassanpour, A., Ghadiri, M., 2014. A linear model of elasto-plastic and adhesive contact deformation. Granul. Matter 16, 151–162.
Savage, S.B., 1979. Gravity flow of cohesionless granular materials in chutes and channels. J. Fluid Mech. 92, 53–96.

Savage, S.B., McKeown, S., 1983. Shear stresses developed during rapid shear of concentrated suspensions of large spherical-particles between concentric cylinders. J. Fluid Mech. 127, 453–472.

Savage, S.B., Sayed, M., 1984. Stresses developed by dry cohesionless granular materials sheared in an annular shear cell. J. Fluid Mech. 142, 391–430.

Savkoor, A.R., Briggs, G.A.D., 1977. Effect of tangential force on contact of elastic solids in adhesion. P. Roy. Soc. Lond. Ser. A. Math. Phys. Eng. Sci. 356, 103–114.

Schulze, D. A new ring shear tester for flowability and time consolidation measurements, 1st International Particle Technology Forum, Denver, USA, 1994, 11–16.

Tabor, D., 2000. The Hardness of Metals. Oxford University Press, Oxford.

Tardos, G.I., Mcnamara, S., Talu, I., 2003. Slow and intermediate flow of a frictional bulk powder in the Couette geometry. Powder Technol. 131, 23–39.

Thornton, C., Yin, K.K., 1991. Impact of elastic spheres with and without adhesion. Powder Technol. 65, 153–166.

Wang, C., Hassanpour, A., Ghadiri, M., 2008. Characterisation of flowability of cohesive powders by testing small quantities of weak compacts. Particuology 6, 282–285.

Zhu, H.P., Zhou, Z.Y., Yang, R.Y., Yu, A.B., 2008. Discrete particle simulation of particulate systems: a review of major applications and findings. Chem. Eng. Sci. 63, 5728–5770.